



High entropy alloys as strain-sensitive materials

S.A. Uporov^{a,*}, I.V. Evdokimov^a, R.E. Ryltsev^a, E.V. Sterkhov^a, V.A. Bykov^a, V.A. Sidorov^b, N.M. Chtchelkatchev^{a,b}

^a Institute of Metallurgy, Ural Branch of Russian Academy of Sciences, Amundsena Str. 101, 620016, Ekaterinburg, Russia

^b Vereshchagin Institute for High Pressure Physics, Russian Academy of Sciences, 108840, Troitsk, Moscow, Russia



ARTICLE INFO

Keywords:

High-entropy alloy
Strain gauge
Structure
Electrical resistivity
Magnetization
Density of states
ab initio calculations

ABSTRACT

Complex concentrated multi-element metallic systems, commonly referred to as high-entropy alloys (HEAs), exhibit a combination of unique physical properties when compared to conventional metallic materials. That makes this class of alloys promising for a variety of functional applications. However, HEAs are too expensive to be used for material-intensive products like structural materials, so their functionality can only be implemented in micro-scale applications. The electrical resistance sensors for detecting and measuring tension stress, pressure, micro-displacements, weight, and other physical parameters seem to be appropriate areas where HEAs could find their own place. This study addresses strain gauge characteristics in several HEAs, such as TiZrHfNb, TiZrHfNbTa, and FeCoCrMnNi (Cantor alloy). We discuss the pressure and strain gauge sensitivities in the systems employing experimentally measured electrical, magnetic, and thermal properties as well as *ab initio* calculations. We conclude that HEAs can be considered as promising materials for strain-sensitive resistance transducers that outperform commercial alloys in terms of a combination of performance characteristics.

1. Introduction

High-entropy alloys (HEAs) discovered almost twenty years ago, have attracted great interest as promising functional materials with unique structure and properties compared to conventional alloys based on one principal metal [1,2]. As is commonly accepted, the increased configurational entropy inherent in such systems makes it possible to stabilize single phase solid solutions with a simple crystalline structure of BCC, FCC, or HCC symmetry [3–6]. In some cases, however, these alloys can crystallize into intermetallic phases with a Laves-type structure [7–11]. Regardless of what crystalline type is formed, all HEAs have irregular and highly defective crystal lattices because they consist of atoms of different radii and valences. The density of various structural defects in HEAs is similar to that observed in severely deformed and nanostructured materials. Such a defective structure is considered to be the reason responsible for achieving improved strength and plasticity, as well as high electrical resistance, which is weakly dependent on temperature. There are several high-resistance HEAs such as Cantor alloy and its derivatives [12–16], as well as refractory ones [17–20] that exhibit virtually constant resistivity over a large temperature span. This property is of pivotal importance if an alloy is used as an electrical sensor or resistor.

Recently, we examined pressure effects on electrical resistivity on the example of TiZrHfNb refractory HEA [21] and found that the alloy has a large baric response comparable to that for managnine, the alloy widely utilized in pressure and strain gauges. This observation encourages us to further examine the pressure and tension effects in HEAs of this class to test whether these effects are exclusive to a certain alloy composition or may be a common feature of these systems. Besides collecting physical data and assessing the functional prospects mentioned, it is also necessary to understand and interpret the experimental observations. The following obvious questions arise along the way. What is the fundamental difference between physical mechanisms behind changes in electrical conductivity under pressure and stress in single-component substances and such chemically complicated systems as HEAs? Is there some atypical electron or phonon contribution that can significantly affect the electron transport properties of these materials? Can we describe strain and pressure resistance effects in HEAs using simple classical free electron models, or do we have to construct some more complicated theory for this purpose? This study is an attempt to address these issues by performing experimental and theoretical study of several popular single-phase HEAs with BCC and FCC crystalline structures, such as TiZrHfNb, TiZrHfNbTa and FeCoCrMnNi (Cantor alloy). To achieve this purpose, we examine the structure of the systems by X-ray

* Corresponding author.

E-mail address: segga@bk.ru (S.A. Uporov).

diffraction, optical and electron microscopy and measure their specific heat, thermal expansion, density, magnetization, and electrical resistance. To construct an adequate model describing electron transport in the HEAs, we inspect possible electron transport scenarios and various structure-property relationships and also perform *ab initio* calculations of electronic structure.

2. Experimental and calculation details

We fabricated HEA samples by arc-melting of appropriate amounts of pure metals (better than 99.99 wt%) taken in an equimolar ratio. The ingots were remelted ten times to ensure chemical homogeneity. Strain gauge materials are usually exploited in a cold-rolled state, and so we fabricated foil samples for the tension tests with a thickness of about 200 μm by applying rolling deformation of as cast samples with about 98 % thickness reduction.

Crystal structure and microstructure of the HEAs were characterized using X-ray diffraction analysis (a Shimadzu XRD-7000 diffractometer with CuK α -radiation), optical (a LOMO MMU-3 metallurgical microscope equipped with a CCD SONY ICX452AQ camera), and electron microscopy (a Carl Zeiss EVO 40 microscope equipped with an INCA-energy EDS X-ray Microanalysis analyzer). The specific heat of the samples was measured with DSC 214 Polyma calorimeter in the temperature range of 100–520 K. The thermal expansion coefficient was measured with Netzsch 402 CD dilatometer. Magnetization of the HEAs was studied using a Cryogenic CFS-9T-CVTI measurement system in a temperature interval of 300–77 K. The baric effects of the electrical resistivity were measured by the four-probe method in the temperature range of 77–300 K under applied hydrostatic pressures of 0–5.41 GPa. These experiments were made in a miniature toroid-type profiled anvil cell equipped with a teflon capsule filled with liquid, as described in detail in Ref. [22]. The resistance-tension tests have been performed on a simple home-built (DIY) PC-controlled device consisting of a pair of load-bearing platforms that set the stress/elongation, and a four-probe resistance recorder connected to a DC source Keithley K2400 and a nanovoltmeter Keithley K2182. Before use, the apparatus has been calibrated with a series of standard strain alloys; the estimated error in determining the strain gauge factor (GF) is about ± 10 %.

To study the electronic structure of HEAs, we utilize density functional theory (DFT) calculations as implemented in VASP code [23]. For the exchange correlation functional, we apply r2SCAN Meta-Generalized Gradient Approximation [24]. Extended versions of projector augmented wave (PAW) pseudopotentials [25] including p – or s – semi-core states as valence states were used for all chemical elements. The energy cutoff of 600 eV was set in all calculations. Sampling of the Brillouin zone was performed using optimal generalized Monkhorst-Pack grids [26,27] generated using KpLib library [28]. We use a k -points grid with the minimum allowed distance between lattice points on the real-space superlattice $r_{\min} = 32 \text{ \AA}$, which provides average accuracy for metallic systems of about 5 meV/atom [26]. Calculations were performed for cubic supercells of 250 atoms (50 atoms of each element), which were randomly seeded on the sites of BCC lattice. Each configuration was relaxed at target pressure, and then calculations of electronic structure were performed. To take into account the effects of compositional disorder, we perform calculations for 10 different random configurations and then average the resulting characteristics (pressure, densities of states, etc.). We also checked that this procedure gives results similar to those obtained with Special Quasirandom Structure (SQS) (see inset in Fig. 8a).

3. Results

3.1. Structural and microstructural analysis

X-ray diffraction patterns of the as-cast and cold-rolled alloys are presented in Fig. 1. According to Le Bail fitting of experimental XRD data

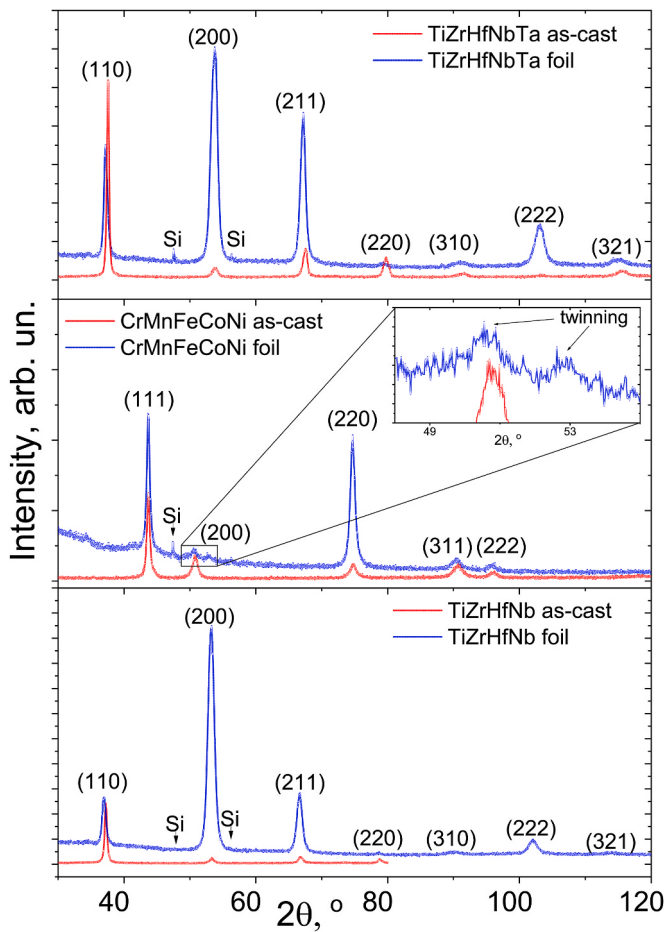


Fig. 1. X-ray diffraction patterns of the as-cast and cold-rolled foil samples of the HEAs. The compositions and kind of the examined alloy samples are given at the corresponding legends in each panel. The inset in the middle panel illustrates an enlarged fragment of the XRD pattern of Cantor's cold-deformed foil, demonstrating the twinning effects discussed in the text. The labels "Si" indicate reflections from the silicon powder that we use here as a reference standard.

performed with the FullProf Suite software package, all the samples can be characterized as single-phase solid solutions with the unit cell parameters listed in Table 1. As expected, TiZrHfNb and TiZrHfNbTa crystallize into the $I\bar{m}\text{-}3m$ BCC phase, and FeCoCrMnNi crystallizes into the $F\bar{m}\text{-}3m$ FCC one. Being subjected to severe mechanical processing (the thickness is reduced by about 98 % from the original cross section), the cold-rolled samples demonstrate a strong texture. In the case of the BCC alloys, we find preferable texturing along $\{200\}$ plane, while the deformed Cantor sample exhibits it within $\{220\}$ direction. Another interesting feature found for the cold-rolled Cantor alloy is the appearance of specific diffraction peaks in the $\{001\}$ family of planes, see the inset in Fig. 1. Perhaps this structural feature is related to the development of long stacking faults or crystal twinning during the deformation

Table 1

Lattice parameters of the as-cast* and cold-rolled foil** samples of the fabricated HEAs according to Le-Bail refinement.

sample	space group	$a, \text{\AA}$	$R_p, \%$	$R_{wp}, \%$
FeCoCrMnNi*	$F\bar{m}\text{-}3m$	3.5961(2)	12.4	16.2
TiZrHfNb*	$I\bar{m}\text{-}3m$	3.4490(5)	10.7	14.2
TiZrHfNbTa*	$I\bar{m}\text{-}3m$	3.3962(1)	9.98	13.2
FeCoCrMnNi**	$F\bar{m}\text{-}3m$	3.5994(5)	5.56	7.28
TiZrHfNb**	$I\bar{m}\text{-}3m$	3.4393(2)	4.27	5.62
TiZrHfNbTa**	$I\bar{m}\text{-}3m$	3.4106(1)	5.6	7.9

process. As has been established in Ref. [29], all these effects actually take place in the Cantor alloy even at the early stages of plastic deformation. Further, we examined the microstructure of the samples using optical and electron microscopy techniques (see Fig. 2). As follows from the pictures, the optical imaging provides better visualization of the structural morphology formed during crystallization as well as cold-rolling processes. Before micrographs were taken, the samples were mechanically polished and etched in a solvent mixture of alcohol and HF acid to achieve a slightly pitted surface. Since dendrites are chemically inhomogeneous in volume, pitting processes caused by etching expose the edges of the dendrites, which makes it possible to visually determine their shape even in the case of barely noticeable segregation of elements observed in the HEAs under study. As a result, we reveal that all the as-cast samples have a dendritic microstructure with randomly oriented crystals several microns in size. The Cantor alloy has the finest dendrites, whereas the refractory alloys have enlarged ones. Note that there are no parasitic inclusions or secondary phases in the samples.

According to SEM-EDX mapping performed, the overall actual chemical compositions of the alloys are very close to the nominal ones within the probe resolution. The EDX scanning through the dendrites and interdendritic regions reveals a subtle dispersion in chemical composition towards light or heavy elements. So we find that the core parts of the dendrites in the refractory alloys are slightly enriched (by % 2–3) in Nb and Ta, while the dendritic edges are enriched to the same extent in Ti and Zr. In the case of Cantor HEA, the element segregation along and across the dendrites is less than % 1, which is typical in this system. After cold-rolling, the microstructure of the alloys is characterized by highly elongated crystallites, deformed in the direction of the mechanical processing. No additional segregation of elements was detected after such a mechanical treatment. Thus, based on these findings, we conclude that the fabricated samples are single-phase disordered solid solutions with a pronounced dendritic microstructure.

3.2. Thermal and magnetic properties

Before considering the effects of pressure and elastic strain on electron transport in the HEAs under study, let us consider some related physical properties. Namely, we examine thermal expansion, specific heat, and magnetization to check whether phase transitions are possible over the operating temperature range. Besides that, these measurements

allow us to extract important parameters needed to interpret the resistivity data of the inspected alloys. The specific heat of the HEAs measured in the range of 100–550 K indicates that there are no evident phase transitions or abnormal deviations in the temperature dependence $C(T)$ (Fig. 3); it reveals the usual behavior typical for a metallic solid. Given this fact, we can apply a standard Debye model corrected by a linear term (βT) that takes into account conduction electron and anharmonic contributions:

$$C(T) = 9R \left(\frac{T}{\Theta_D} \right)^3 \int_0^{\Theta_D/T} \frac{e^x x^4}{(e^x - 1)^2} dx + \beta T, \quad (1)$$

here R is the gas constant and Θ_D is the Debye temperature. The best fits of experimental data by eq. (1) yield the following Θ_D values: 350 K for the Cantor alloy, 250 K for TiZrHfNb and 218 K for TiZrHfNbTa. The linear coefficient (β) in all systems is of the order of $6 \text{ mJ}/(\text{molK}^2)$, which is typical for transition metals and alloys. The Θ_D parameters extracted from the $C(T)$ curves are in well agreement with those obtained in other

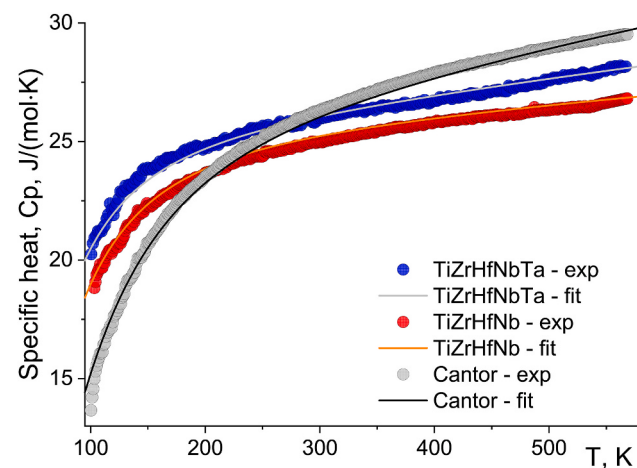


Fig. 3. Specific heat of the as-cast HEAs vs. temperature. The dots correspond to experimental data, the solid lines represent the fitting curves with the Debye model.

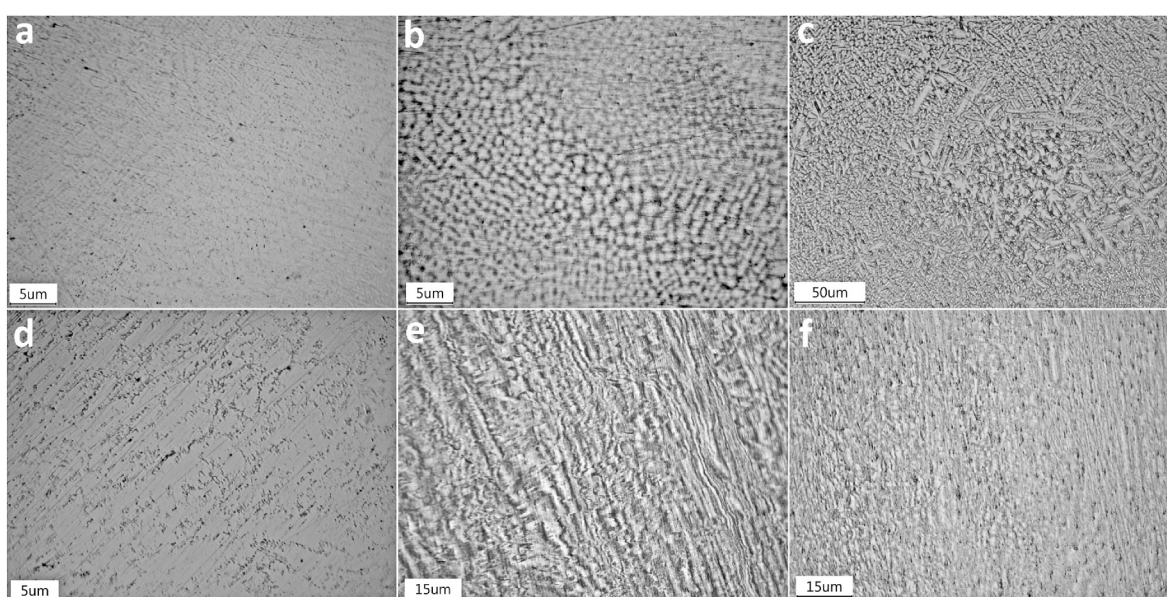


Fig. 2. Optical micrographs of the as-cast (a, b, c) and cold-rolled foil (d, e, f) samples of the fabricated high entropy alloys: Cantor alloy (a, d); TiZrHfNb (b, e); and TiZrHfNbTa (c, f).

studies [30–32] and can therefore be used in further analysis. The thermal expansion $\Delta l/l_0$ measured in the HEAs exhibits a strictly linear temperature dependence, indicating a constant coefficient of thermal expansion $d(\Delta l/l_0)/dT$ (CTE) over a wide temperature interval. The estimated CTEs for TiZrHfNb and TiZrHfNbTa are very close, with values of $(7.5\text{--}8.0) \times 10^{-6} \text{ K}^{-1}$ in the temperature interval between 300 K and 550 K. In contrast, in the same temperature range, the Cantor alloy has a higher CTE, which is about $(15\text{--}17) \times 10^{-6} \text{ K}^{-1}$.

The experimentally defined structural and thermal properties of the HEAs allow us to calculate the Grüneisen parameter γ_G at ambient conditions [33]:

$$\gamma_G = \frac{3\alpha BV_0 N_A}{C_V}, \quad (2)$$

where α is CTE, B is the bulk modulus taken for each alloy from this review [34], V_0 is the primitive unit cell volume, N_A is the Avogadro number, and C_V is the molar constant-volume heat capacity taken to be close to the measured isochoric one, i.e., $C_V \approx C_p$. The resulted γ_G coefficients are 1.72 for FeCoCrMnNi, 1.88 for TiZrHfNb and 1.44 for TiZrHfNbTa. These estimates are quite reasonable and consistent well with those available for these systems [35,36], and thus we can take these γ_G values as input data for subsequent analysis of the electron transport properties in the HEAs.

The magnetic susceptibility has been measured between room temperature and liquid nitrogen one, as shown in Fig. 4. We see that the studied HEAs are weak paramagnets that do not exhibit magnetic ordering down to 77 K. Weak magnetic response and the absence of specific electronic or structural transitions are of great importance for functional materials. The main difference between the systems under investigation is that the refractory HEAs are Pauli-like phases with temperature-independent magnetism, whereas the Cantor alloy demonstrates Curie-like behavior. Taking into account the mentioned classes of magnetic systems, we fit the obtained data with the appropriate free-electron models to extract some electronic characteristics. The susceptibility of Cantor alloy is fitted by the modified Curie-Weiss law, $\chi(T) = \Delta + C/(T - \theta)$, where the terms used have their standard meanings. In the case of the refractory HEAs, we approximate the magnetic data with the temperature-corrected Pauli susceptibility, written as $\chi(T) = \chi_0 + aT^2$ [37]. The derived constants allow us to calculate the effective magnetic moment per atom μ_{eff} and the electron density of states (DOS) at the Fermi level $n(E_F)$ using the following equations: $\mu_{\text{eff}} = 2.83\sqrt{M \times C}$ where M is molar mass and the DOS $n(E_F) = \chi_p/(2\mu_0\mu_B^2 S)$, where μ_0 is the

magnetic constant and S is the Stoner exchange parameter taken as 1.5, χ_p is the Pauli susceptibility extracted from χ_0 by correcting for the Van Vleck paramagnetic and Landau diamagnetic contributions (see Ref. [38] for technical details). We found that Cantor alloy has μ_{eff} as large as $1.36 \mu_B$, while TiZrHfNb and TiZrHfNbTa alloys have no localized magnetic moments. Due to the large response from the local moments and other electronic contributions, it is difficult to correctly estimate DOS in the Cantor system from magnetization data. These estimates made for TiZrHfNb and TiZrHfNbTa lead to more or less reasonable DOS values of about 1.5 and 1.8 eV^{-1} , respectively, which agree with results of *ab initio* calculations (see Fig. 8). As for the DOS of the Cantor alloy, here we can refer to the DFT calculations made by Elmslie et al. [30], where it has been established as $n(E_F) = 1.349 \text{ eV}^{-1}$. Given these findings, we can conclude that such a high electron occupation implies a predominance of the *d*-bands at the Fermi energy and therefore provides a significant contribution of the *d*-electrons to magnetism and electron transport in the systems under consideration.

3.3. Electrical resistivity vs. T and P

The effects of temperature and hydrostatic pressure on the electrical resistance ρ of the examined HEAs are illustrated in Figs. 5 and 6. We see that the resistivity of the HEAs is quite high and weakly dependent on temperature. The temperature dependence $\rho(T)$ exhibits a positive slope, indicating a metallic type of conductivity. Temperature coefficients of resistance (TCR) as small as $(0.1\text{--}5.4) \times 10^{-4} \text{ K}^{-1}$, which is a typical case for concentrated alloys of this class [12–20]. Note that there is a significant difference in resistivity and TCR between TiZrHfNb and TiZrHfNbTa. The higher resistivity with near-zero TCR in the TiZrHfNb alloy is due to more pronounced average species-resolved atomic displacements compared to those in TiZrHfNbTa [17]. Similar electrical properties have been observed in Constantan and Manganin, popular functional alloys that are widely used as resistors and tension transducers. The lower the TCR, the better a material meets the functional requirements for such applications. Anyway, the main property of a sensor is its sensitivity, and thus it is also extremely important to understand how and to what extent its physical characteristics can change under different conditions. As follows from the derived baric dependencies $\rho(P)$, the pressure coefficients of the relative resistance $\frac{1}{\rho_0} \frac{\partial \rho(P)}{\partial P}$ are negative but fairly large in magnitude. The pressure coefficients of the resistance are $-2.31 \times 10^{-5} \text{ MPa}^{-1}$, $-2.06 \times 10^{-5} \text{ MPa}^{-1}$, and $-1.75 \times 10^{-5} \text{ MPa}^{-1}$ for TiZrHfNb, TiZrHfNbTa, and Cantor alloy, respectively. These values are very close in magnitude to those observed in Manganin, see Refs. [39,40]. Compared to the anomalous positive baric response in manganin, the pressure coefficients of

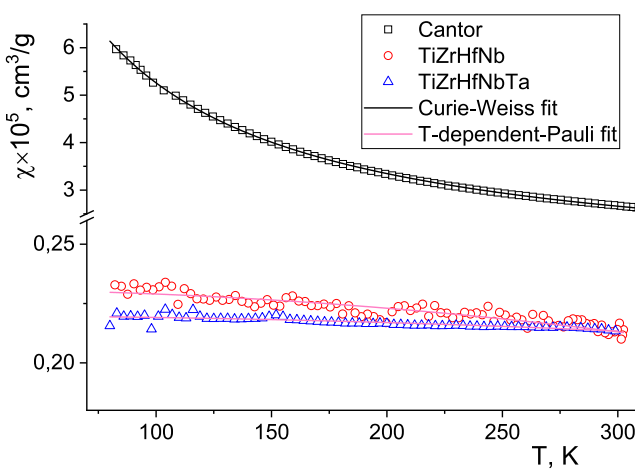


Fig. 4. Magnetic susceptibility of the as-cast HEAs vs. temperature. The dots correspond to experimental data, the solid lines represent the fitting curves with the Curie-Weiss law (Cantor alloy) and the T-corrected Pauli law (the refractory alloys).

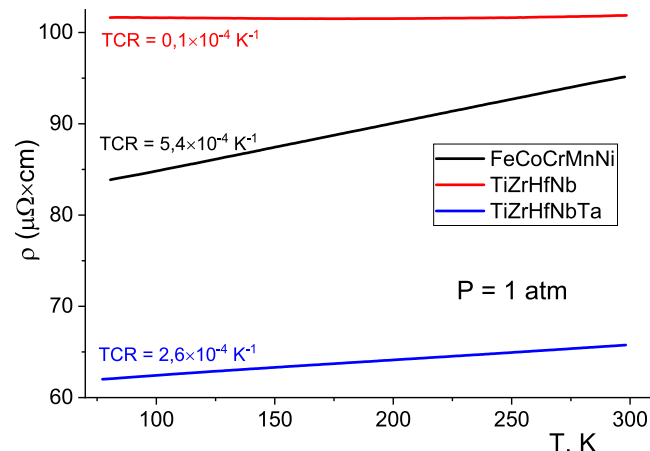


Fig. 5. Electrical resistivity of the as-cast HEAs vs. temperature, measured at ambient pressure. TCR - temperature coefficients of resistivity.

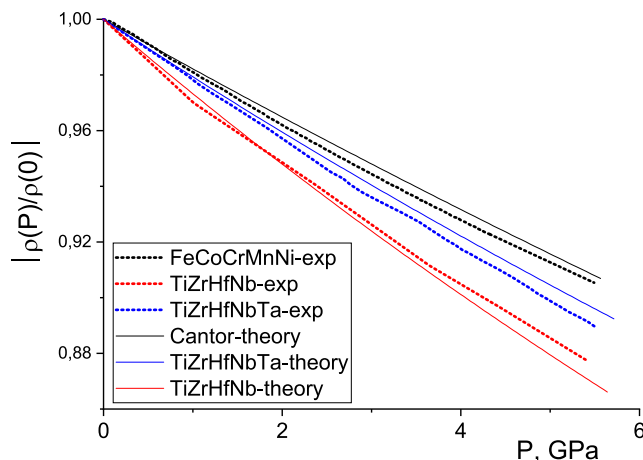


Fig. 6. Relative baric changes in electrical resistivity at $T = 295$ K, defined as $|\rho(P)/\rho_0|$, where $\rho(P)$ and ρ_0 are the resistivity at applied and ambient pressure, respectively. Data points - the experiment, solid curves are the theoretical expectations, as predicted by the model described in the text.

resistivity in the HEAs are negative, as in the case of most metals and alloys. These findings indicate that electron transport in these complex solid solutions may be somewhat similar to that in simple metals [41]. So we see there is no atypical behavior in the resistivity change under pressure in the case of the HEAs.

3.4. Electrical resistivity vs. elastic deformation

Further, we consider the effects of elastic deformation on the resistance of the HEAs under study. Due to the fact that most real metallic strain gauges are made from cold-rolled foil, strain gauge sensitivity tests have been carried out on such foil samples. In Fig. 7 we show relative resistivity $\Delta R/R_0$ as a function of strain ϵ for the cold-rolled HEAs. We see that the resistivity of the examined alloys reveals strictly linear changes under applied stress within the overall elastic range. The gauge factor of the HEAs, defined as $GF = \Delta R/R_0\epsilon$, is quite large ($GF = 3.49\text{--}4.78$) compared to that for commonly used strain gauge alloys such as Constantan ($GF = 2.0\text{--}2.2$) and Manganin ($GF =$

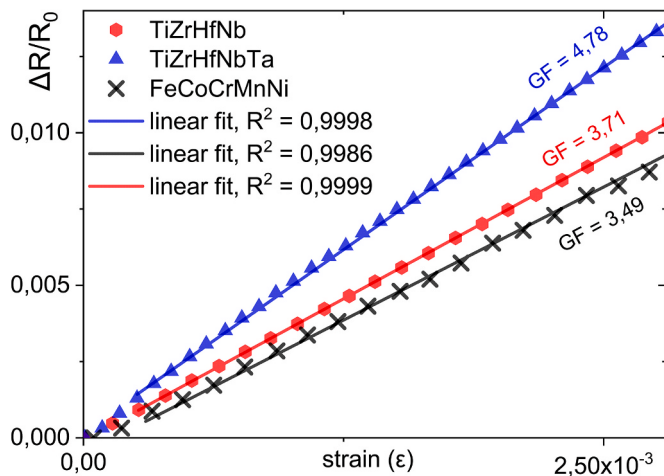


Fig. 7. Relative resistivity $\Delta R/R_0$ vs. strain ϵ for the cold-rolled HEAs listed in the legend, measured at ambient temperature and pressure. Ultimate stress values at the maximum ϵ correspond to 764 MPa for TiZrHfNb, 782 MPa - TiZrHfNbTa, and 890 MPa - FeCoCrMnNi. The points represent the experimental data, solid curves - linear approximation. The GF values provided denote the gauge factor derived for the examined samples (highlighted in the same color as the corresponding data).

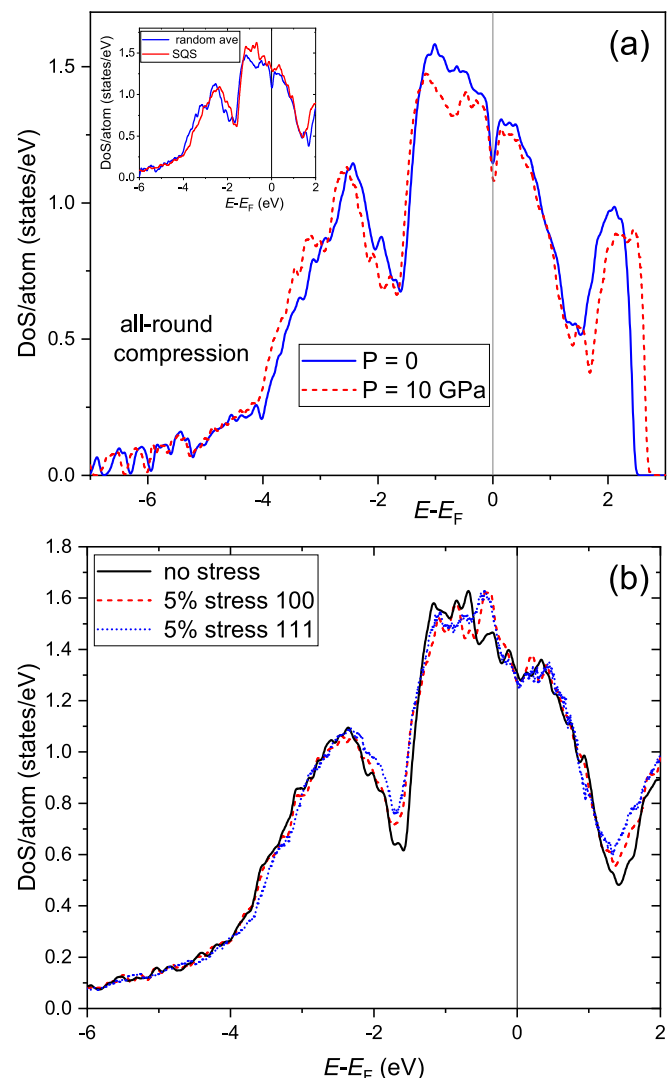


Fig. 8. Total electronic density of states (DOSs) for TiZrHfNbTa HEA obtained via *ab initio* calculations. (a) Main frame: comparison of DOSs at zero pressure with that calculated at $P = 10$ GPa. Inset: comparison of DOS calculated by averaging over 10 random distributions of atoms on lattice sites with that obtained for SQS. (b) Effect of 5 % stretching of the lattice along $\{100\}$ and $\{111\}$ directions on total DOS.

0.5–0.7) [42,43].

3.5. Electronic structure

To get deeper insight into the physical mechanisms of the resistivity and validate the conclusions made after analysis of experimental data, we perform *ab initio* calculations of the electronic structure of TiZrHfNb and TiZrHfNbTa alloys subjected to all-round compression as well as 5 % stretching along $\{100\}$ and $\{111\}$ directions. In Fig. 8, we present calculated total electronic densities of states (DOSs) for TiZrHfNbTa alloy (the results for TiZrHfNb are very similar). We see that both compression and stretching have little effect on DOSs. No substantial dependence of stretched samples DOSs on the stress direction is observed. These results support the idea that observed pressure/tension effects are rather caused by lattice deformations than by changes in electronic structure.

4. Discussion and conclusions

4.1. Mechanisms of pressure and strain dependencies of resistivity

The above experimental observations suggest that the HEAs under investigation demonstrate the same mechanisms of electronic transport as conventional metallic alloys. Thus, we can use standard models based on classical scattering mechanisms for interpreting the obtained dependencies of resistivity on both all-round compression and strain. We start our discussion with a more simple case of HEAs under hydrostatic pressure. A simple approach describing $\rho(P)$ curves was recently reported for the TiZrHfNb alloy [21]. The model is based on the assumption that the alloy's resistance is determined mainly by two contributions, such as residual resistance (Drude term) and s - d scattering resistance (Mott term). It is worth noting that temperature effects are basically related to the Drude resistivity (the alloy resistivity weakly depends on T), while pressure effects are found to be strongly associated with the s - d scattering mechanisms. The details of these speculations can be found in Ref. [21]. Here we will use the resulted formulas to check whether the proposed approach is universal for describing the baric effects in HEAs.

We express the resistance ρ_{total} of HEAa as a sum of the residual (ρ_{res}) and the Mott (ρ_{sd}) resistance terms. When modeling resistance-pressure curves, only those terms that depend on pressure are taken into account; the rest are included in the P -independent constants α and β . The final resistance equations used for modeling are as follows:

$$\rho_{\text{total}} = \rho_{\text{res}} + \rho_{\text{sd}} \sim \alpha N(E_F) + \beta \frac{N(E_F)}{\Theta_D^2}, \quad (3)$$

where $N(E_F)$ is the DOS at the Fermi level and Θ_D is the Debye characteristic temperature.

We see from eq. (3) that the baric behavior of resistance in HEAs is determined by pressure variations of both $N(E_F)$ and Θ_D . Thus, it is necessary to know the pressure dependencies for these parameters to simulate $\rho(P)$ curve. Our *ab initio* calculations performed at different pressures show that the DOS changes by no more than 2.5 % under an applied pressure of 5.5 GPa (see Fig. 8a). If we take these data as input into equation (3), we get a similar decrease in resistance. As one can see, the overall changes in the alloy resistance under the same pressure are as large as 10–12.5 %. Obviously, observed pressure variations of DOSs are too minor to explain the resistance behavior and can even be neglected. Changes in the Debye temperature caused by lattice compression appear to have a much more significant effect on the resistivity under pressure than the DOS variations. In order to define the $\Theta_D(P)$ function, we use a well-known classical model based on the Grüneisen parameter γ_G [33] and the third-order Birch-Murnaghan equation of state [44] that relates the unit cell volume and pressure via bulk modulus B and its pressure derivative B' as follows:

$$\Theta_D(V) = \Theta_D^0 \left(\frac{V}{V_0} \right)^{\gamma_G}, \quad (4)$$

$$P(V) = \frac{3}{2} B \left[\left(\frac{V}{V_0} \right)^{-\frac{7}{3}} - \left(\frac{V}{V_0} \right)^{-\frac{5}{3}} \right] \times \left\{ 1 + \frac{3}{4} (B' - 4) \left[\left(\frac{V}{V_0} \right)^{-\frac{2}{3}} - 1 \right] \right\}. \quad (5)$$

Taking experimental assessments for γ_G coefficients and ambient pressure Debye temperatures as well as the bulk modules calculated through *ab initio* simulations, we find the $\Theta_D(P)$ functions for each studied HEA. Once we get these functions, we simulate a model curve describing the resistivity behavior with pressure using equation (3) and taking the coefficients $\alpha = 0$ and $\beta = 1$. Note that such values of α and β

were adopted to highlight the predominant role of the Mott contribution (s - d scattering mechanism) to pressure effects in the alloy resistance. The results of the calculations are shown in Fig. 6 by dotted lines. We see good agreement between calculated and experimental dependencies, and thus it is enough to take into account only the change in Θ_D to semi-quantitatively describe the change in resistance under pressure in these complex systems. As seen in Fig. 6, the maximum deviation between the simulated Mott resistance and the experimental dots is about 0.7 %, which is close to the measurement uncertainty. Obviously, if we take into account the changes in DOS and calculate the values of α and β , then a perfect approximation of the resistance-pressure curves would be provided. Note that here we are not striving for a perfect fit but rather looking for a more or less reasonable explanation of the observations to shed some light on the nature of the physical mechanisms responsible for electron transport in these complex alloys. The performed analysis allows us to conclude that the suggested expression (3) is fairly adequate to quantitatively describe the pressure effects in HEAs under investigation.

Let us now discuss a more complicated case of resistivity behavior under strain. Note that strain gauge sensitivity in metallic materials has been discussed for many decades, but many questions still remain unresolved. As is known, the GF is commonly expressed as a sum of two main contributions:

$$GF = \frac{\Delta R/R_0}{\epsilon} = [1 + 2\nu] + \left[\frac{\Delta \rho/\rho}{\epsilon} \right], \quad (6)$$

where ϵ is the strain or relative elongation ($\Delta l/l$), ν is the Poisson's ratio. The first term $[1 + 2\nu]$ represents a geometrical effect of deformation, and the second one is related to the changes in specific resistance under strain. Since ν in most metals is usually around 1/3, the purely geometrical contribution to GF is not expected to be more than 2. Thus, a high strain gauge sensitivity of some alloys, including the HEAs under study, is due to abnormal changes in their resistivity. Unfortunately, there is no universal equation describing the resistivity under tension, despite many decades of research [45–51]. There are many non-trivial issues that complicate the solution of this problem. Indeed, the elastic stress causes uneven lattice deformation, which can result in a lowering of the crystal lattice symmetry. As a consequence, anisotropic effects arising from elongation must also be taken into account. Such effects are very hard to measure and control experimentally, which makes it difficult to estimate their contributions to the overall resistivity. Besides that, it is necessary to understand which of the resistance contributions discussed above play a major role in the strain gauge sensitivity.

The residual resistance is assumed to be independent on pressure, so it seems reasonable to further consider it as a term weakly dependent on elastic strain. As is commonly accepted, the Drude conductivity is basically related to the density of structural defects. In the first approximation, we can assume that the lattice defectiveness of a metal is an intrinsic characteristic that is invariable with respect to pressure or tension stress. If this is true, the s - d scattering mechanism appears to be responsible for the abnormal increase in resistivity when stress is applied to such an alloy.

As we pointed out above, the Mott resistance (see eq. (6)) vs. pressure is mainly determined by variations in both the DOS and the Debye temperature. *Ab initio* calculations show that DOS changes weakly under stress (see Fig. 8) and so we expect that the main contribution to the GF is due to variations of the Debye temperature under deformation. The direct calculation of Θ_D as a function of strain is a complicated task, and so the detailed discussion of this dependence is out of the scope of this paper. However, we believe that this problem can be solved by computational methods that will open new perspectives for effectively predicting GF in HEAs.

4.2. Perspectives of using HEAs as strain-sensitive materials

Summing up the study findings, let us speculate about the possible applicability of some HEAs in connection with the strain effects observed. We believe that such metallic materials may be suitable for creating new strain gauges with better sensitivity and linearity characteristics. When considering a particular alloy for use as a real sensor, one should keep in mind its overall functionality and take into account all advantages and drawbacks. There are some physical and engineering aspects worth noting here. The first one is that the sensitivity factor in HEAs is remarkable, but it is similar to that established in some Fe-based (3.5–6) [52–56] and Pt-based (4–6) [47,57–61] strain gauge alloys. The former materials exhibit strong magnetic response and nonlinearity, while the latter are good in functionality but too expensive for widespread use. Besides the mentioned systems, there are a great number of strain-sensitive alloys with large GF. However, many of them have various disadvantages with respect to other functional characteristics required for real sensors (thermal stability, fatigue life, operating temperature range, electromotive force, CTE, TCR, and many others). Selecting a suitable strain gauge alloy is usually a compromise between several properties to satisfy particular constraints or requirements. All this explains why Constantan, Manganin, Nichrom, and other well-known commercial alloys possessing moderate GF are widely utilized as strain gage alloys; they have the finest overall mix of characteristics. A primary screening throughout the examined properties shows that the HEAs can be considered as promising materials for strain-sensitive resistance transducers, see Table 2.

5. Conclusions

The effects of pressure and elastic deformation on the electrical resistance of TiZrHfNb, TiZrHfNbTa and FeCoCrMnNi (Cantor alloy) high entropy alloys have been studied for the first time. The main outcomes of this research are as follows.

- (1) The pressure coefficients of the relative resistance $\frac{1}{\rho_0} \frac{\partial \rho(P)}{\partial P}$ are found to be negative but fairly large in magnitude. The basic dependencies are successfully described within the framework of the proposed simple model, which takes into account only two contributions, such as residual resistance (Drude term) and $s-d$ scattering resistance (Mott term).
- (2) The resistivity of the examined alloys reveals strictly linear changes under applied stress. The defined strain gauge factor (GF) is found to be as large as GF = 3.49–4.78, compared to that of commonly used commercial strain gauge alloys such as Constantan (GF = 2.0–2.2) and Manganin (GF = 0.5–0.7). Based on the analysis of the results, we make the assumption that the high strain gauge sensitivity in the HEAs is mainly due to a drastic change in their the Debye temperature Θ_D that occurs during elastic tension.
- (3) The DFT calculations show that the electronic structure of the HEAs changes weakly under stress and pressure. The variations in the DOS are too small to be taken into account to interpret the effects of pressure and tension on the resistivity in the systems.
- (4) Analysis of the examined properties allows us to conclude that high entropy alloys have a unique combination of mechanical and electronic properties, which allows them to be considered as promising materials for strain-sensitive resistance transducers.

CRediT authorship contribution statement

S.A. Uporov: Writing – original draft, Supervision, Project administration, Data curation, Conceptualization. **I.V. Evdokimov:** Visualization, Methodology, Investigation. **R.E. Ryltsev:** Writing – review & editing, Writing – original draft, Investigation, Formal analysis, Data

Table 2

The strain gauge factor (GF), the pressure coefficient of relative resistance (PCR) and the coefficient of thermal expansion (CTE) of the investigated HEAs, as determined under room temperature conditions.

composition	GF	PCR	CTE
	($\pm 10\%$)	($\times 10^5$, MPa $^{-1}$)	($\times 10^6$, K $^{-1}$)
FeCoCrMnNi	3.49	1.75	15
TiZrHfNb	3.71	2.31	7.5
TiZrHfNbTa	4.78	2.06	7.5

curation. **E.V. Sterkhov:** Visualization, Validation, Methodology, Investigation. **V.A. Bykov:** Visualization, Methodology, Investigation, Formal analysis. **V.A. Sidorov:** Methodology, Investigation. **N.M. Chchelkatchev:** Investigation, Formal analysis, Conceptualization.

Declaration of competing interest

The authors declare that they have no known competing financial interests or personal relationships that could have appeared to influence the work reported in this paper.

Data availability

Data will be made available on request.

Acknowledgements

This work was supported by Russian Science Foundation (grant 23-13-00162). Experiments were performed using scientific instruments included in the Collective Equipment Center "Ural-M".

References

- [1] B. Cantor, I.T.H. Chang, P. Knight, A.J.B. Vincent, Microstructural development in equiatomic multicomponent alloys, Mater. Sci. Eng. 375–377 (2004) 213–218. URL: <https://www.sciencedirect.com/science/article/pii/S0921509303009936>.
- [2] J.-W. Yeh, S.-K. Chen, S.-J. Lin, et al., Nanostructured high-entropy alloys with multiple principal elements: novel alloy design concepts and outcomes, Adv. Eng. Mater. 6 (5) (2004) 299–303. <https://onlinelibrary.wiley.com/doi/pdf/10.1002/adem.200300567>.
- [3] Easo P. George, Raabe Dierk, Robert O. Ritchie, High-entropy alloys, Nat. Rev. Mater. 4 (8) (2019, Aug) 515–534, <https://doi.org/10.1038/s41578-019-0121-4>.
- [4] Steurer Walter, Single-phase high-entropy alloys - a critical update, Mater. Char. 162 (2020) 110179. <https://www.sciencedirect.com/science/article/pii/S1044580319329134>.
- [5] M. Claudia Troparevsky, James R. Morris, R.C. Kent Paul, et al., Criteria for predicting the formation of single-phase high-entropy alloys, Phys. Rev. X 5 (2015, Mar) 011041. URL: <https://link.aps.org/doi/10.1103/PhysRevX.5.011041>.
- [6] Wei Chen, Hilhorst Antoine, Bokas Georgios, et al., A map of single-phase high-entropy alloys, Nat. Commun. 14 (1) (2023, May) 2856, <https://doi.org/10.1038/s41467-023-38423-7>.
- [7] S.S. Mishra, T.P. Yadav, O.N. Srivastava, et al., Formation and stability of C14 type Laves phase in multi component high-entropy alloys, J. Alloys Compd. 832 (2020) 153764. URL: <https://www.sciencedirect.com/science/article/pii/S0925838820301274>.
- [8] Anirudha Karati, V.S. Hariharan, Sanyukta Ghosh, et al., Thermoelectric properties of half-Heusler high-entropy $Ti_2NiCoSn_{1-x}Sb_{1+x}$ ($x = 0.5, 1$) alloys with $VEC > 18//$ Scripta, Materialia 186 (2020) 375–380. URL: <https://www.sciencedirect.com/science/article/pii/S1359646220302669>.
- [9] Ostovari Moghaddam Ahmad, Fereidonnejad Rahele, Naseri Majid, et al., Synthesis and characterization of novel high entropy Heusler intermetallics, Intermetallics 159 (2023) 107917. URL: <https://www.sciencedirect.com/science/article/pii/S096979523000973>.
- [10] N. Yurchenko N. Stepanov, G. Salishchev, Laves-phase formation criterion for high-entropy alloys, Mater. Sci. Technol. 33 (1) (2017) 17–22, <https://doi.org/10.1080/02670836.2016.1153277>.
- [11] Ryltsev Roman, Gaviko Vasiliy, Estemirova Svetlana, et al., Laves phase formation in high entropy alloys, Metals 11 (12) (2021). URL: <https://www.mdpi.com/2075-4701/11/12/1962>.
- [12] K. Jin, B.C. Sales, G.M. Stocks, et al., Tailoring the physical properties of Ni-based single-phase equiatomic alloys by modifying the chemical complexity, Sci. Rep. 6 (1) (2016, Feb) 20159, <https://doi.org/10.1038/srep20159>.
- [13] Sai Mu, German D. Samolyuk, Wimmer Sebastian, et al., Uncovering electron scattering mechanisms in NiFeCoCrMn derived concentrated solid solution and

- high entropy alloys, *npj Comput. Mater.* 5 (1) (2019. Jan) 1, <https://doi.org/10.1038/s41524-018-0138-z>.
- [14] Chou Hsuan-Ping, Chang Yee-Shyi, Chen Swe-Kai, Jien-Wei Yeh, Microstructure, thermophysical and electrical properties in $\text{Al}_x\text{CoCrFeNi}$ ($0 \leq x \leq 2$) high-entropy alloys, *Mater. Sci. Eng. B* 163 (3) (2009) 184–189. URL: <https://www.sciencedirect.com/science/article/pii/S09215107090002438>.
- [15] Yanwen Zhang, Stocks G. Malcolm, Ke Jin, et al., Influence of chemical disorder on energy dissipation and defect evolution in concentrated solid solution alloys, *Nat. Commun.* 6 (1) (2015) 8736, <https://doi.org/10.1038/ncomms9736>. Oct.
- [16] Ke Jin, Hongbin Bei, Single-phase concentrated solid-solution alloys: bridging intrinsic transport properties and irradiation resistance, *Frontiers in Materials* 5 (2018). URL: <https://www.frontiersin.org/articles/10.3389/fmats.2018.00026>.
- [17] Sai Mu, S. Wimmer, S. Mankovsky, et al., Influence of local lattice distortions on electrical transport of refractory high entropy alloys, *Scripta Mater.* 170 (2019) 189–194. URL: <https://www.sciencedirect.com/science/article/pii/S1359646219303008>.
- [18] Yaguang Dong, Sai Mu, Xun Guo, et al., Transport properties of refractory high-entropy alloys with single-phase body-centered cubic structure, *Scripta Mater.* 231 (2023) 115464. URL: <https://www.sciencedirect.com/science/article/pii/S1359646223001884>.
- [19] S. Vrtnik, P. Koželj, A. Meden, et al., Superconductivity in thermally annealed Ta-Nb-Hf-Zr-Ti high-entropy alloys, *J. Alloys Compd.* 695 (2017) 3530–3540. URL: <https://www.sciencedirect.com/science/article/pii/S0925838816339907>.
- [20] N.K. Sarkar, C.L. Prajapat, P.S. Ghosh, et al., Investigations on superconductivity in an equi-atomic disordered Hf-Nb-Ta-Ti-V high entropy alloy, *Intermetallics* 144 (2022) 107503. URL: <https://www.sciencedirect.com/science/article/pii/S096697552000449>.
- [21] S.A. Uporov, R.E. Ryltsev, V.A. Sidorov, et al., Pressure effects on electronic structure and electrical conductivity of TiZrHfNb high-entropy alloy, *Intermetallics* 140 (2022) 107394. URL: <https://www.sciencedirect.com/science/article/pii/S096979521003101>.
- [22] Alla E. Petrova, A. Sidorov Vladimir, M. Stishov Sergei, High-pressure helium gas apparatus and hydrostatic toroid cell for low-temperatures applications//Physica B: condensed Matter, Proceedings of the International Conference on Strongly Correlated Electron Systems 359–361 (2005) 1463–1465. URL: <https://www.sciencedirect.com/science/article/pii/S0921452605004850>.
- [23] G. Kresse, J. Furthmüller, Efficiency of ab-initio total energy calculations for metals and semiconductors using a plane-wave basis set, *Comput. Mater. Sci.* 6 (1) (1996) 15–50. <http://www.sciencedirect.com/science/article/pii/0927025696000080>.
- [24] James W. Furness, Aaron D. Kaplan, Jinliang Ning, et al., Accurate and numerically efficient r2SCAN meta-generalized gradient approximation, *J. Phys. Chem. Lett.* 11 (19) (2020) 8208–8215. Oct.
- [25] G. Kresse, D. Joubert, From ultrasoft pseudopotentials to the projector augmented-wave method, *Phys. Rev. B* 59 (1999. Jan) 1758–1775. URL: <https://link.aps.org/doi/10.1103/PhysRevB.59.1758>.
- [26] Pandu Wisesa, Kyle A. McGill, Tim Mueller, Efficient generation of generalized Monkhorst-Pack grids through the use of informatics//Phys. Rev. Bus. 93 (2016. Apr) 155109. URL: <https://link.aps.org/doi/10.1103/PhysRevB.93.155109>.
- [27] Yunze Wang, Wisesa Pandu, Balasubramanian Adarsh, et al., Rapid generation of optimal generalized Monkhorst-Pack grids, *Comput. Mater. Sci.* 187 (2021) 110100.
- [28] KpLib – open-sourced C++ library for searching and generating optimal generalized k-point grids for efficient integration in reciprocal space during electronic structure calcualtions. <https://muellergroup.jhu.edu/K-Points.html>. Accessed: 2024-March-25.
- [29] Oliveros Daniela, Fraczkiewicz Anna, Dlouhy Antonin, et al., Orientation-related twinning and dislocation glide in a cantor high entropy alloy at room and cryogenic temperature studied by in situ TEM straining, *Mater. Chem. Phys.* 272 (2021) 124955. URL: <https://www.sciencedirect.com/science/article/pii/S0254058421007380>.
- [30] Timothy A. Elmslie, Jacob Startt, Sujeily Soto-Medina, et al., Magnetic properties of equiatomic CrMnFeCoNi, *Phys. Rev. B* 106 (2022. Jul) 014418. URL: <https://link.aps.org/doi/10.1103/PhysRevB.106.014418>.
- [31] Y.X. Ye, B.L. Musico, Z.Z. Lu, et al., Evaluating elastic properties of a body-centered cubic NbHfZrTi high-entropy alloy - a direct comparison between experiments and ab initio calculations, *Intermetallics* 109 (2019) 167–173. URL: <https://www.sciencedirect.com/science/article/pii/S0966979518311245>.
- [32] Uttam Bhandari, Ghadimi Hamed, Congyan Zhang, et al., Computational exploration of biomedical HfNbTaTiZr and Hf0, 5Nb0.5Ta0.5Ti1.5Zr refractory high-entropy alloys //Mater. Res. Express 8 (9) (2021. sep) 096534, <https://doi.org/10.1088/2053-1591/ac1d65>.
- [33] Grimvall Göran, Chapter 8 – PHONONS IN real crystals: ANHARMONIC EFFECTS// thermophysical properties of materials, in: GÖRAN GRIMVALL, Elsevier Science B. V., Amsterdam, 1999, 136–152, <https://www.sciencedirect.com/science/article/pii/B9780444827944500097>.
- [34] Yuanyuan Shang, Brechtl Jamieson, Pistidda Claudio, Peter K. Liaw, in: Jamieson Brechtl, Peter K. Liaw (Eds.), Mechanical Behavior of High-Entropy Alloys: A Review//High-Entropy Materials: Theory, Experiments, and Applications, Springer International Publishing, Cham, 2021, pp. 435–522, https://doi.org/10.1007/978-3-030-77641-1_10, 978-3-030-77641-1.
- [35] James A. Stewart Jacob K. Startt, Dingreville Remi, A molecular dynamics study on the Mie-Grüneisen equation-of-state and high strain-rate behavior of equiatomic CoCrFeMnNi, *Materials Research Letters* 11 (12) (2023) 1055–1062, <https://doi.org/10.1080/21663831.2023.2280635>.
- [36] K. Jasiewicz, B. Wiendlocha, K. Górnicka, et al., Pressure effects on the electronic structure and superconductivity of $(\text{TaNb})_{0.67}(\text{HfZrTi})_{0.33}$ high entropy alloy, *Phys. Rev. B* 100 (2019. Nov) 184503. URL: <https://link.aps.org/doi/10.1103/PhysRevB.100.184503>.
- [37] John MD. Coey, in: Magnetism and Magnetic Materials, Cambridge university press, 2010, <https://doi.org/10.1017/CBO9780511845000>.
- [38] S. Uporov, V. Bykov, S. Estemirova, Electrical and thermal conductivities of rapidly crystallized Cu-Zr alloys: the effect of anharmonicity, *Phys. B Condens. Matter* 499 (2016) 97–106. URL: <https://www.sciencedirect.com/science/article/pii/S0921452616302885>.
- [39] Christopher Armstrong, Philip Rae, Tasker Doug, et al., Inexpensive method of qualifying piezoresistive thin-film pressure gauges, *AIP Conf. Proc.* 1979 (1) (2018) 160001. <https://aip.scitation.org/doi/pdf/10.1063/1.5045000>.
- [40] Zhuoping Duan, Liu Yan, Pi Aiguo, Fenglei Huang, Foil-like manganin gauges for dynamic high pressure measurements, *Meas. Sci. Technol.* 22 (7) (2011. jun) 075206, <https://doi.org/10.1088/0957-0233/22/7/075206>.
- [41] Frank D. Stacey, L. Anderson Orson, Electrical and thermal conductivities of Fe-Ni-Si alloy under core conditions, *Phys. Earth Planet. In.* 124 (3) (2001) 153–162. URL: <https://www.sciencedirect.com/science/article/pii/S0031920101001868>.
- [42] K. Rajanna, M.M. Nayak, Strain Sensors//Wiley Encyclopedia of Electrical and Electronics Engineering, John Wiley & Sons, Ltd, 1999, ISBN: 9780471346081, <https://onlinelibrary.wiley.com/doi/pdf/10.1002/047134608X.W4000>.
- [43] Strain Gages - Introduction to Electrical Strain Gages//Experimental Mechanics of Solids, John Wiley & Sons, Ltd, 2012, pp. 41–73. ISBN: 9781119994091, <https://onlinelibrary.wiley.com/doi/pdf/10.1002/9781119994091.ch3>.
- [44] Francis Birch, Finite elastic strain of cubic crystals//phys. Rev. E. 71 (1947. Jun) 809–824. URL: <https://link.aps.org/doi/10.1103/PhysRev.71.809>.
- [45] P.W. Bridgman, The effect of tension on the thermal and electrical conductivity of metals, *Proc. Am. Acad. Arts Sci.* 59 (6) (1923) 119–137. URL: <http://www.jstor.org/stable/20026069>. (Accessed 13 March 2024).
- [46] P.W. Bridgman, The effect of tension on the electrical resistance of certain abnormal metals, *Proc. Am. Acad. Arts Sci.* 57 (3) (1922) 41–66. URL: <http://www.jstor.org/stable/20025885>. (Accessed 13 March 2024).
- [47] Viness Irwin, Investigation of stress-strain relations of metal wires by electrical resistance changes, *J. Appl. Phys.* 23 (1) (1952) 43–47, 01, https://pubs.aip.org/aip/jap/article-pdf/23/1/43/18311062/43_1_online.pdf.
- [48] M. Brauwers, F. Brouers, Temperature and strain effect on electrical resistivity of transition metal alloys: application to strain gauges, *J. Phys. F Met. Phys.* 6 (7) (1976. jul) 1331, <https://doi.org/10.1088/0305-4608/6/7/014>.
- [49] G.C. Kuczynski, Effect of elastic strain on the electrical resistance of metals, *Phys. Rev.* 94 (1954. Apr) 61–64. URL: <https://link.aps.org/doi/10.1103/PhysRev.94.61>.
- [50] Z.H. Meiksin, R.A. Hudzinski, A theoretical study of the effect of elastic strain on the electrical resistance of thin metal films, *J. Appl. Phys.* 38 (11) (1967) 4490–4494, 10, https://pubs.aip.org/aip/article-pdf/38/11/4490/18343358/4490_1_online.pdf.
- [51] W.A. Rees David, The sensitivity of strain gauges when used in the plastic range, *Int. J. Plast.* 2 (3) (1986) 295–309. URL: <https://www.sciencedirect.com/science/article/pii/0749641986900057>.
- [52] Mikio Yamamoto, Takuho Nakamichi, Norio Yokoyama, Norikuni Hayashi, Strain gauge factor and electrical and magnetic properties in as-coldworked state of iron-nickel-chromium alloys containing 35 wt.% nickel and 0 ~ 20 wt.% chromium// science reports of the research institutes, Tohoku University. Ser. A, Physics, Chemistry and Metallurgy 18 (0) (1966) 486–493. <https://cir.nii.ac.jp/crid/1570854176988276992>.
- [53] Masumoto Hakaru, Saito Hideo, Nakamura Naoji, Strain gauge factor and electrical properties of Fe-Co-Mn alloys, *Transactions of the Japan Institute of Metals* 15 (2) (1974) 139–142, <https://doi.org/10.2320/matertrans1960.15.139>.
- [54] Masumoto Hakaru, Naoji Nakamura, Effect of heat treatment on the strain gauge factor of the Fe-Cr-Co system, *Transactions of the Japan Institute of Metals* 19 (6) (1978) 335–340, <https://doi.org/10.2320/matertrans1960.19.335>.
- [55] Masumoto Hakaru, Nakamura Naoji, The strain gauge factor and electrical properties in a cold-worked state of iron-chromium alloys, *Transactions of the Japan Institute of Metals* 10 (2) (1969) 124–127, <https://doi.org/10.2320/matertrans1960.10.124>.
- [56] Masumoto Hakaru, Naoji Nakamura, Effect of addition of cobalt or nickel on the strain gauge factor and electrical properties of iron-chromium alloys, *Transactions of the Japan Institute of Metals* 10 (2) (1969) 128–131, <https://doi.org/10.2320/matertrans1960.10.128>.
- [57] R. Bertoldi, Development of high-temperature strain gauges, *Proc. Inst. Mech. Eng.* 173 (1) (1959) 605–622, https://doi.org/10.1243/PIME_PROC_1959_173_052_02.
- [58] R. Bertoldi, Precious metal alloys for high-temperature resistance strain gauges, *J. Phys. Appl. Phys.* 1 (12) (1968) 1743, <https://doi.org/10.1088/0022-3727/1/12/321>, dec.
- [59] J.W. Pitts, D.G. Moore, Development of High-Temperature Strain Gages, National Institute of Standards and Technology, Gaithersburg, MD, 1961, 10.6028/NBS.MONO.26.
- [60] Lizhen Tong, Jinxing Guo, Noble metal alloys as strain gauge materials, URL: <http://www.ingentacollect.com/content/matthey/pmr/1994/00000038/00000003/art00001/>, 1994.
- [61] Jinxing Guo, Lizhen Tong, Lihua Chen, Platinum alloy strain gauge materials, *Platin. Met. Rev.* 41 (1) (1997) 24–32. URL: <https://technology.matthey.com/content/journals/10.1595/003214097X4112432>.